RSC Advances

PAPER

View Article Online
View Journal | View Issue

Check for updates

Cite this: *RSC Adv.*, 2021, **11**, 2892

Enhanced anti-*Escherichia coli* properties of Fe-doping in MgO nanoparticles†

Xiaoyu Hong, Yan Yang, * Xiaoyi Li, Maurice Abitonze, Catherine Sekyerebea Diko, Jiao Zhao,* Qiao Ma, Weifeng Liu and Yimin Zhu*

Received 11th November 2020
Accepted 1st January 2021

DOI: 10.1039/d0ra09590g

rsc.li/rsc-advances

Hetero-elements doping is an effective way to modify the composition and nanostructure of metal oxides. These modifications could lead to changes in physical and chemical properties correspondingly. In this study, Fe-doped MgO nanoparticles (NPs) were synthesized by simple calcination method in air. The antibacterial activity of MgO NPs against *Escherichia coli* (*E. coli*, ATCC 25922) was significantly improved as shown by the bactericidal efficacy test results. According to X-ray diffraction (XRD) results, Fe was successfully doped into MgO lattice and mainly adopted interstitial doping. The Fe-doping led to increased oxygen vacancies and O_A content (from 13.5% to 41.3%) on MgO surface, which may have facilitated the reactive oxygen species (ROS) generation and bacteria death. The wrinkled and sunken *E. coli* surface after contact with Fe-doped MgO NPs also confirmed the existence of adsorption damage mechanism. Thus, the antibacterial activity enhancement against *E. coli* was originated from the synergistic effect of increased ROS concentration and the interaction with Fe-doped MgO NPs.

Open Access Article. Published on 14 January 2021. Downloaded on 2/9/2026 1:03:30 PM.
This article is licensed under a Creative Commons Attribution-NonCommercial 3.0 Unported Licence.

1. Introduction

Human beings are suffering from Corona Virus (COVID-19) now. Beside viruses, other pathogenic microorganisms such as bacteria and fungi[1] can also cause infectious diseases which can also cause global deaths.[2] Antibacterial agents are effective to destroy or inhibit bacterial activities and improve environmental sanitation for the benefit of human health.[3] Various inorganic, organic and biological antibacterial agents have been explored in recent times.[4] Among them, inorganic antibacterial agents (such as metal ions and oxides) have increasingly attracted attention due to their advantages such as high selectivity, superior durability, heat resistance and chemical stability.[5–7] Until now, variable metal ions have been explored and proven to be effective inorganic antibacterial agents, *i.e.* Ag^{+}, Hg^{2+}, Cu^{2+}, Cd^{2+}, Cr^{3+}, Ni^{2+}, Pb^{2+}, Zn^{2+}, $Fe^{3+}$and Ti^{4+}.[1,8–13] However, most of these are heavy metal ions are not only expensive but also very toxic to human beings if largely used in sanitary products. MgO has attracted intensive interests due to its large reserves, low cost, readily availability, economical precursors, high thermal stability and low toxicity to human beings.[14,15] MgO has been widely applied in medicine and antibacterial agents and it has exhibited significant inhibition properties on many bacteria, such as *Escherichia coli*, *Salmonella typhimurium*, *Pseudomonas aeruginosa*, *Staphylococcus aureus* and *Bacillus subtilis*.[15–19] Many reports have focused on the antibacterial properties of MgO and developed various strategies to improve its antibacterial ability. For instance, through different synthesis method to control its particle sizes,[20] using surfactants[21] and other functional groups to modify its surface properties,[22,23] manipulating its elemental compositions through hetero-elements doping[24] (*i.e.* Li, Ca, Zn, Ti, Cu and Ag), or producing new complexes with other nano materials like multi-walled carbon nanotubes (MWNTs)[25] and graphene.[26] Reducing the particle sizes of MgO can increase its surface area and enhance the ROS generation in solution, leading to a more effective destruction of the bacterial cell wall. Thus, decreasing the particle sizes of MgO is an effective way to improve its antibacterial activity. Besides size control, hetero-atom doping has been proved to be a convenient and valid way to alter MgO's properties and raise its antibacterial ability. This is due to the increase in oxygen vacancy content that is generated during hetero-element's substitution in MgO matrix. Until now, Li, Ca, Zn, Ti, Cu and Ag elements have been successfully doped into MgO through one-pot synthesis or post treatment methods.[8] Compared with others, Ag and Cu showed superior antibacterial ability and high toxicity levels.[27] Therefore, new hetero-elements doping in MgO with high antibacterial activity but low toxicity to both human and environment needs to be developed.

In our previous research, magnesium-based antibacterial materials were investigated and mainly focused on antibacterial nanomaterials and fabrics.[28,29] Here, novel Fe-doped MgO NPs were successfully prepared through post treatment calcination method. The findings indicated that, when doped with

Collaborative Innovation Center for Vessel Pollution Monitoring and Control, Dalian Maritime University, Dalian 116026, China. E-mail: yyang@dlmu.edu.cn; zhaojiao@dlmu.edu.cn; ntp@dlmu.edu.cn

† Electronic supplementary information (ESI) available. See DOI: 10.1039/d0ra09590g

© 2021 The Author(s). Published by the Royal Society of Chemistry

Open Access Article. Published on 14 January 2021. Downloaded on 2/9/2026 1:03:30 PM.
This article is licensed under a Creative Commons Attribution-NonCommercial 3.0 Unported Licence.

some amount of Fe *i.e.* 0.11 wt%, the antibacterial properties of MgO NPs against *E. coli* were greatly enhanced. XRD and high-resolution transmission electron microscopy (HRTEM) results showed that the presence of Fe did not disturb the crystal structure of MgO NPs and mainly acted as interstitial impurity which could be beneficial in activating oxygen and ROS generation. X-ray photoelectron spectroscopy (XPS) and photoluminescence (PL) results further supported the above hypothesis with significant increase in chemisorbed oxygen (O_A) content from 13.5% to 41.3% and oxygen defects concentration in Fe-doped MgO NPs. Scanning Electron Microscope (SEM) images showed that the enhanced antibacterial property originated from the synergetic effect of increased ROS concentration and interaction with Fe-doped MgO NPs.

2. Experimental section

2.1 Chemicals and reagents

Magnesium oxide (MgO) and ferrous chloride ($FeCl_2$) of analytical grade were obtained from Tianjin Kemiou Chemical Reagent Company and were used as supplied.

2.2 Preparation of Fe-doped MgO nanoparticles

The samples preparation were carried out as follows: the MgO powder was ball-milled for 30 min. The MgO powder was mixed with various amounts of $FeCl_2$. The mixtures were ground and heated to 1000 °C at a heating rate of 10 °C min^{-1}. This temperature was maintained for 2 h in air to yield calcined samples. The total concentration was 50 mmol with x ($x = 0$, 0.4 and 1.2) mmol of $FeCl_2$, and the samples were denoted as MgO, Fe–MgO-1 and Fe–MgO-2 respectively.

2.3 Characterization

To understand the Fe-doping effect on MgO, the Fe-doped MgO NPs were characterized to assess their structural, optical, and morphological properties. The X-ray analysis of all samples were carried out by a X Pert PRO diffractometer with CuKα (λ = 1.5406 Å) radiation, 2θ range of 5–90 degrees. The atomic compositions of MgO and Fe–MgO were determined using inductively coupled plasma optical emission spectrometer (ICP-OES, Perki-nElmer ICP Optima 7000DV). Scanning electron microscopy (SEM) and XPS analysis of the samples were performed by Hitachi S4600 and Thermo VG, respectively. PL spectra of the powdered NPs were observed by spectrofluorometer (HoribaJobin Yvon) and Transmission Electron Microscopy (TEM) images were received by using a JEM 2100f TEM with an acceleration voltage of 200 kV.

2.4 Antibacterial test

To evaluate antibacterial properties of the as-obtained samples, *E. coli* ATCC 25922 was selected as a model.[26] The bactericidal efficacy was tested as follows: 0.1 mL of the bacterial solutions at a concentration of 0.75 mg mL^{-1} were taken and plated in sterile nutrient agar plates. The plates were then incubated at 37 °C for 24 h.[30] After the incubation period, the number of bacteria colonies formed were counted. The bactericidal rate (K) was calculated as follows:[31]

$$K = (A - B)/A \times 100\%$$

In the equation, A and B are the number of bacterial colonies in positive control group and sample groups, respectively.

3. Results and discussions

XRD spectra of the undoped and Fe-doped MgO nanoparticles are shown in Fig. 1. All the peaks corresponded to the cubic MgO nanoparticles (111), (200), (220), (311), (222) which are in accordance with the Inorganic Crystal Structure Database (ICSD) card number 00-45-0946 and no other peaks were observed. Hence, the Fe-doping did not disturb the crystal structure of MgO nanoparticles and Fe atoms might have been well doped into the MgO lattice. The inset in Fig. 1 showed the enlarged (200) peak of all samples. The peak at (200) of Fe-doped MgO samples shifted gradually to the left with the increase in Fe content which could be due to the Fe dopant. The lattice calculations of (200) peaks are shown in Table 1. The interplanar distance (d) of the samples were determined according to Bragg's law. Compared with MgO (4.2049 Å) lattice, the lattice parameters of Fe–MgO-1 and Fe–MgO-2 increased slightly to 4.2099 Å and 4.2170 Å respectively, indicating the interstitial Fe doping was dominant.

To reveal the composition of Fe doped MgO NPs samples, the contents of Fe in solution were determined by ICP-OES analysis. It showed a linear increase with the initial $FeCl_2$ quantities from 0.11 to 0.75 wt% (Table 1). Combined with the XRD results, Fe elements had entered the framework of MgO and mainly occupied the interstitial sites of MgO during re-crystallization

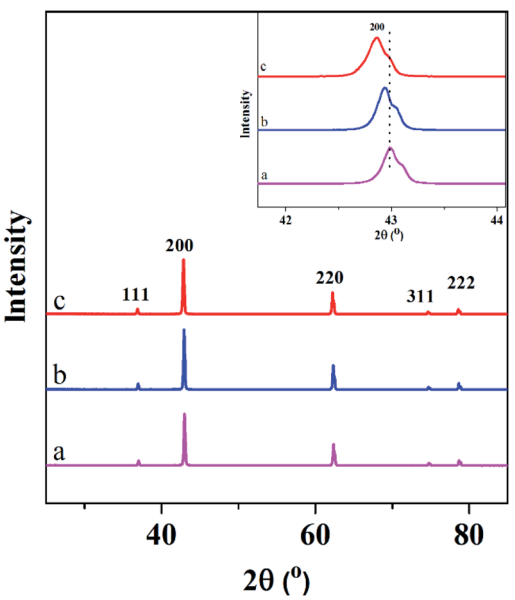

Fig. 1 XRD patterns of the MgO NPs (a) and Fe-doped MgO NPs samples: Fe–MgO-1 (b) and Fe–MgO-2 (c).

Open Access Article. Published on 14 January 2021. Downloaded on 2/9/2026 1:03:30 PM.
This article is licensed under a Creative Commons Attribution-NonCommercial 3.0 Unported Licence.

Table 1 XRD data of the MgO NPs and Fe-doped MgO NPs samples

Samples	2 Theta (°)	*d*-Spacing (Å)	FWHM (°)	Crystallite size (nm)	*a* (Å)	Fe content (wt%)	Bactericidal rate *K* (%)
MgO NPs	43.037	2.1000	0.194	43.6	4.2049	0	>99.99
Fe–MgO-1	42.919	2.1055	0.179	47.2	4.2099	0.11	>99.99
Fe–MgO-2	42.852	2.1094	0.196	43.1	4.2170	0.75	>99.99

process.[32] The morphologies and nanostructures of the representative sample Fe–MgO-1 and control MgO NPs were investigated by high-resolution scan electron microscopy (HRSEM), TEM and HRTEM respectively. As shown in Fig. 2A and B, both MgO NPs and Fe–MgO-1 displayed nanoparticles with average particle sizes of ~200 nm. Compared with MgO NPs, Fe–MgO-1 showed smoother surface probably due to the high temperature calcination procedure (1000 °C). The TEM images confirmed the particle sizes of MgO NPs and Fe–MgO-1 (Fig. 2C–F). HRTEM and high angle annular dark-field scanning transmission electron microscope (HAADF-STEM, Fig. 2E, F, 3A and B) analysis were performed to further identify the microstructure of samples. The interplanar spacing observed in Fig. 2E and F are ~0.169 nm and ~0.210 nm and they matched with the (111) and (200) crystal plane of MgO NPs respectively. These corresponded well with d-spacing calculated from XRD. The Fe–MgO-1 sample showed no metallic Fe and other material phases (Fig. 2F). To further learn the Fe distribution in Fe–MgO-1, elemental mapping was conducted. As shown in Fig. 3C–E, the Mg, O and Fe are dispersed homogeneously within Fe–MgO-1. These results indicate that, there might have been a successful incorporation of Fe element into MgO lattice which is in accordance with the XRD results.[33]

The antibacterial properties of Fe-doped MgO samples were evaluated using *E. coli* ATCC 25922 as a model. Fig. 4 shows the representative photographs for the antibacterial activities of pure MgO NPs and Fe-doped MgO NPs samples at a concentration of 0.75 mg mL^{-1}. After contacting MgO NPs for 24 h, few bacteria survived compared to the positive control. The bacterial colony number in Fig. 4A–D were 8.3×10^7 CFU mL^{-1}, 1.3×10^4 CFU mL^{-1}, 1×10^3 CFU mL^{-1}, 9×10^2 CFU mL^{-1} respectively. Fe-doped MgO NPs showed better antibacterial performance with less bacterial colonies observed in the plates compared with control MgO NPs. The Fe–MgO-1 also showed much higher antibacterial activities than our previously reported MgO materials, as shown in Fig. S2.†[35]

To explore the reason for antibacterial activity increment, XPS, PL and HRSEM characterizations were adopted. The XPS survey spectra of MgO NPs and Fe-doped MgO NPs are displayed in Fig. 5. The high resolution O1s XPS spectra of Fe–MgO-1 and Fe–MgO-2 are shown in Fig. 5C and D. The O1s peaks of each sample was divided into two subpeaks centered at 529.3 and 531.5 eV, those were assigned to lattice oxygen (O_L) and (O_A) respectively. Based on XPS data, compared to MgO NPs (13.5%, Fig. S1†), the molar percentage of O_A in O species increased largely to 38.9% and 41.3% for Fe–MgO-1 and Fe–

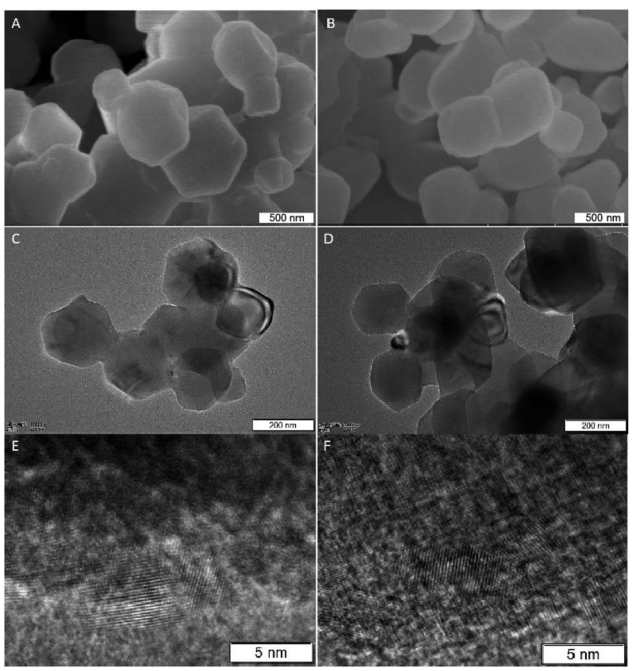

Fig. 2 HRSEM, TEM and HRTEM images of MgO NPs (A, C and E) and Fe–MgO-1 (B, D and F).

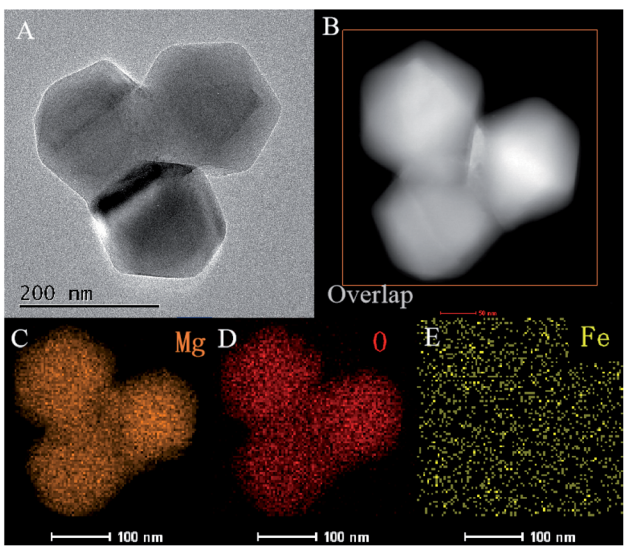

Fig. 3 HRTEM image of Fe–MgO-1 (A), HAADF-STEM image of Fe–MgO-1 (B), Mg, O and Fe mapping (C–E) of rectangle area in image B.

© 2021 The Author(s). Published by the Royal Society of Chemistry

Open Access Article. Published on 14 January 2021. Downloaded on 2/9/2026 1:03:30 PM.
This article is licensed under a Creative Commons Attribution-NonCommercial 3.0 Unported Licence.

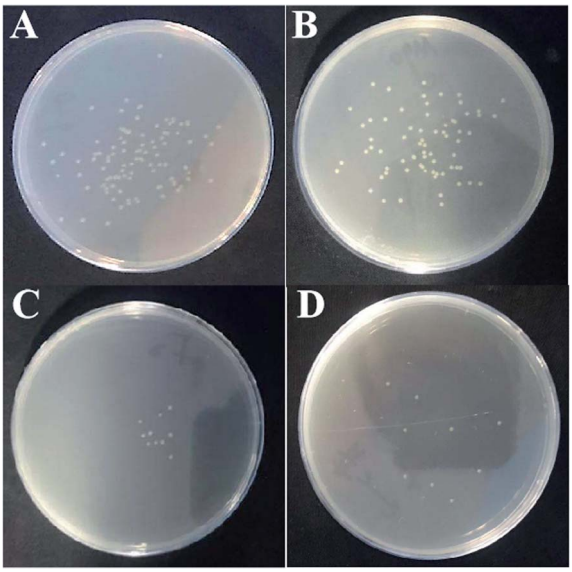

Fig. 4 Bactericidal activities of samples with the concentration of 0.75 mg mL^{-1}, (A) positive control (10^6 CFU mL^{-1}); (B) MgO NPs (10^2 CFU mL^{-1}); (C) Fe–MgO-1 (10^2 CFU mL^{-1}); (D) Fe–MgO-2 (10^2 CFU mL^{-1}).

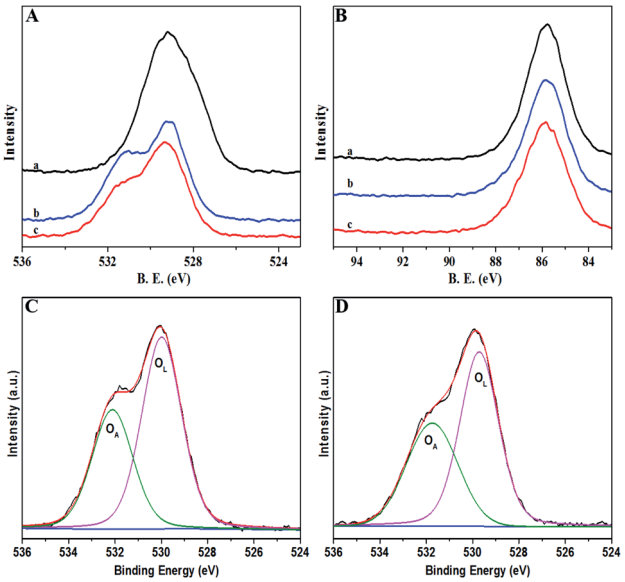

Fig. 5 XPS survey spectra of samples for (a) MgO NPs, (b) Fe–MgO-1, (c): Fe–MgO-2; (A): high resolution O 1s, (B): high resolution Mg 2s, C-D: O 1s XPS spectra of Fe–MgO-1 and Fe–MgO-2, respectively.

MgO-2 respectively.[34] Moreover, the oxygen vacancy had strong adsorption ability towards oxygen. Thus, the highly improved O_A contents in Fe-doped MgO samples were mostly caused by the increase in oxygen vacancy concentration. All three samples showed similar crystallite sizes, hence the improvement of O_A content mainly originated from Fe-doping.

In order to identify oxygen vacancy concentration, PL measurement was utilized.[36] Room temperature PL spectra of MgO NPs and Fe-doped MgO NPs samples are shown in Fig. 6. All samples exhibited two main emission peaks at 395 nm and 468 nm which were attributed to UV and visible emission respectively.[37] The UV emission was produced by the recombination between electrons and holes, while the visible emission was related to the defects such as oxygen vacancies and Mg interstitials.[38] Thus, the increased intensity of the PL bands in Fe-doped MgO NPs samples suggested that both the density and intensity of sample defects were enhanced together with oxygen vacancies. It is well known that oxygen vacancy has strong activation ability towards chemisorbed oxygen which could be beneficial for the generation of ROS.[38–40] Besides, the alkali microenvironment around the MgO NPs surface was also beneficial for the generation and stabilization of active oxygen (O_2^-).[8,41] ROS is detrimental to bacterial cells due to its high reactivity with amino acids, lipids and proteins *etc*[42]. Compared with MgO NPs, Fe-doped MgO NPs samples exhibited higher O_A content, which was favourable for the generation and stabilization of ROS. Furthermore, Zhang *et al.* used computational simulation method and studied the micro-electronic structure of Fe-doped MgO model. They found that the electronic structure of Fe-doped MgO is easy for electrons jumping and can act as the catalytic active center for activating the adsorbed oxygen or the oxygen in the water, generating radicals and ROS with strong redox ability.[42] Thus, Fe-doping led to significantly enhanced antibacterial inhibition activity.[21,22] To reveal more information about the antibacterial mechanism, surface changes of *E. coli* before and after contact with Fe–MgO-1 NPs were investigated through SEM imaging of dehydrated cells (Fig. 7A and B).[43] As shown in Fig. 7A, the cell surface of *E. coli* was smooth and uniform before antibacterial treatment. However, under Fe–MgO-1 NPs exposure, the cell surface became clearly wrinkled and sunken, suggesting that, there was serious cell damage which was probably caused by the interaction of Fe–MgO-1 NPs with *E. coli.* In combination with the XPS and PL results, the possible antibacterial mechanism for Fe-doped MgO NPs was the synergistic effect of ROS and interaction between Fe-doped MgO NPs and *E. coli.* The possible mechanism illustration is shown in Fig. 8. Compared with MgO NPs, an increased oxygen vacancy and ROS concentrations were obtained through Fe-doping, thus the Fe-doped MgO samples showed enhanced antibacterial activity against *E. coli*.

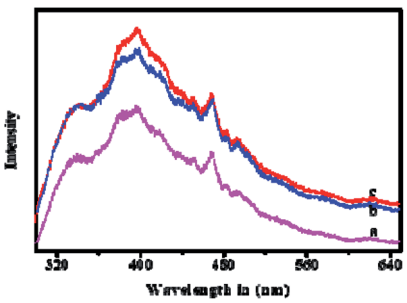

Fig. 6 PL spectra of MgO NPs (a), Fe–MgO-1 (b) and Fe–MgO-2 (c).

Open Access Article. Published on 14 January 2021. Downloaded on 2/9/2026 1:03:30 PM.
This article is licensed under a Creative Commons Attribution-NonCommercial 3.0 Unported Licence.

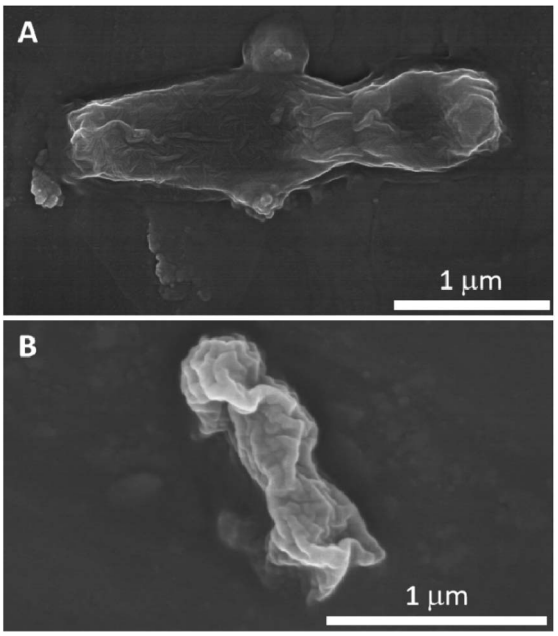

Fig. 7 Typical SEM images of *E. coli* before (A) and after (B) treatment with 0.75 mg mL^{-1} Fe–MgO-1 NPs.

4. Conclusion

Fe-doped MgO NPs with different Fe contents were prepared utilizing simple calcination technique. Fe-doping did not affect the crystal structures and morphologies of MgO NPs but led to increased lattice parameters due to the major interstitial doping. Compared with MgO NPs, the antibacterial properties were greatly enhanced after Fe-doping through bactericidal efficacy test against *E. coli*. XPS and PL results confirmed the formation of Fe-doped MgO NPs and showed largely increased O_A content (from 13.5% to 41.3%) and oxygen vacancies which originated from the improved electronic structure because of Fe doping. The increased oxygen vacancies of Fe-doped MgO NPs as well as the interaction between NPs and *E. coli* all promoted its antibacterial activity synergistically.

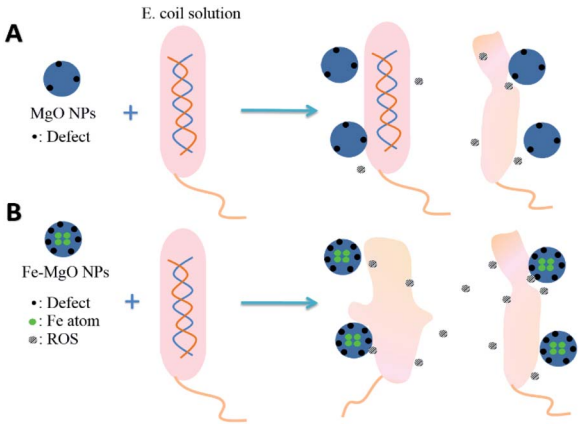

Fig. 8 Possible mechanism illustration of the synergistic effect of ROS and physical interaction between MgO NPs, Fe-doped MgO NPs and *E. coli*.

Conflicts of interest

There are no conflicts to declare.

Acknowledgements

This work was financially supported by Xinghai Program of Dalian Maritime University (02500512), Liaoning Revitalization Talents Program (XLYC1907137) and Fundamental Research Funds for the Central Universities (3132019334).

References

1 V. K. Bajpai, H. R. Kim, C. T. Hou and S. C. Kang, *New Biotechnol.c*, 2009, **26**, 122–130.
2 F. Al-Hazmi, F. Alnowaiser, A. Al-Ghamdi, A. A. Al-Ghamdi, M. Aly, R. M. Al-Tuwirqi and F. El-Tantawy, *Superlattices Microstruct.*, 2012, **52**, 200–209.
3 A. Markowska-Szczupak, K. Ulfig and A. Morawski, *Catal. Today*, 2011, **169**, 249–257.
4 A. Mousavi Khaneghah, S. M. B. Hashemi, I. Eş, D. Fracassetti and S. Limbo, *J. Food Prot.*, 2018, **81**, 1142–1156.
5 V. K. Sharma, R. A. Yngard and Y. Lin, *Adv. Colloid Interface Sci.*, 2009, **145**, 83–96.
6 G. Soto, H. Tiznado, O. Contreras, E. Pérez-Tijerina, J. Cruz-Reyes, M. Del Valle and A. Portillo, *Powder Technol.*, 2011, **213**, 55–62.
7 S. Suwanboon, P. Amornpitoksuk, P. Bangrak and N. Ceram, *Ceram. Int.*, 2013, **5**, 5597–5608.
8 Y. Rao, W. Wang, F. Tan, Y. Cai, J. Lu and X. Qiao, *Appl. Surf. Sci.*, 2013, **284**, 726–731.
9 Z. Jing, *Mater. Sci. Eng., A*, 2006, **441**, 176–180.
10 J. He, I. Ichinose, S. Fujikawa, T. Kunitake and A. Nakao, *Chem. Mater.*, 2002, **14**, 3493–3500.
11 H. Cui, X. Wu, Y. Chen, J. Zhang and R. Boughton, *Mater. Res. Bull.*, 2015, **61**, 511–518.
12 X. Zhu, D. Wu, W. Wang, F. Tan, P. K. Wong, X. Wang, X. Qiu and X. Qiao, *J. Alloys Compd.*, 2016, **684**, 282–290.
13 Y. Cai, D. Wu, X. Zhu, W. Wang, F. Tan, J. Chen, X. Qiao and X. Qiu, *Ceram. Int.*, 2017, **43**, 1066–1072.
14 K. Krishnamoorthy, J. Y. Moon, H. B. Hyun, S. K. Cho and S.-J. Kim, *J. Mater. Chem.*, 2012, **22**, 24610–24617.
15 Y. H. Leung, A. M. Ng, X. Xu, Z. Shen, L. A. Gethings, M. T. Wong, C. M. Chan, M. Y. Guo, Y. H. Ng and A. B. Djurišić, *Small*, 2014, **10**, 1171–1183.
16 M. M. Imani and M. Safaei, *J. Nanotechnol.*, 2019, **2019**, 6063832.
17 S. M. Dizaj, F. Lotfipour, M. Barzegar-Jalali, M. H. Zarrintan and K. Adibkia, *Mater. Sci. Eng., C*, 2014, **44**, 278–284.
18 J. Vidic, S. Stankic, F. Haque, D. Ciric, R. Le Goffic, A. Vidy, J. Jupille and B. Delmas, *J. Nanopart. Res.*, 2013, **15**, 1595.
19 Z.-X. Tang and B.-F. Lv, *Braz. J. Chem. Eng.*, 2014, **31**, 591–601.
20 T. Jaiakumar, M. Umadevi, J. Mayandi and G. Sathe, *Mater. Lett.*, 2016, **184**, 82–87.

© 2021 The Author(s). Published by the Royal Society of Chemistry

Open Access Article. Published on 14 January 2021. Downloaded on 2/9/2026 1:03:30 PM.
This article is licensed under a Creative Commons Attribution-NonCommercial 3.0 Unported Licence.

21 O. Yamamoto, J. Sawai, H. Kojima and T. Sasamoto, *J. Mater. Sci.: Mater. Med.*, 2002, **13**, 789–792.
22 T. Ohira, M. Kawamura, Y. Iida, M. Fukuda and O. Yamamoto, *J. Ceram. Soc. Jpn.*, 2008, **116**, 1234–1237.
23 O. Yamamoto, T. Ohira, K. Alvarez and M. Fukuda, *Mater. Sci. Eng., B*, 2010, **173**, 208–212.
24 C.-Y. Hsieh and K.-Z. Fung, *J. Phys. Chem. Solids*, 2008, **69**, 302–306.
25 Y. Prabhu, K. V. Rao, B. S. Kumari and T. Pavani, *Rendiconti Lincei-Scienze Fisiche E Naturali*, 2015, **26**, 263–270.
26 A. Arshad, J. Iqbal, M. Siddiq, Q. Mansoor, M. Ismail, F. Mehmood, M. Ajmal and Z. Abid, *J. Appl. Phys.*, 2017, **121**, 024901.
27 N. L. Lala, R. Ramaseshan, L. Bojun, S. Sundarrajan, R. Barhate, L. Ying-jun and S. Ramakrishna, *Biotechnol. Bioeng.*, 2007, **97**, 1357–1365.
28 Y. Wang, L. Sha, J. Zhao, Q. Li, Y. Zhu and N. Wang, *Appl. Surf. Sci.*, 2017, **400**, 413–419.
29 Y. Wang, J. Zhao, L. Sha, Y. Zhu and X. Li, *J. Mater. Sci.*, 2018, **53**, 1610–1622.
30 D. Wei, W. Sun, W. Qian, Y. Ye and X. Ma, *Carbohydr. Res.*, 2009, **344**, 2375–2382.
31 T. Liu, H. Tang, X. Cai, J. Zhao, D. Li, R. Li and X. Sun, *Nucl. Instrum. Methods Phys. Res., Sect. B*, 2007, **264**, 282–286.
32 J. Jia, W. Yang, P. Zhang and J. Zhang, *Appl. Catal., A*, 2017, **546**, 79–86.
33 I. Balint and K.-i. Aika, *Appl. Surf. Sci.*, 2001, **173**, 296–306.
34 J. Jia, P. Zhang and L. Chen, *Appl. Catal., B*, 2016, **189**, 210–218.
35 X. Li, J. Zhao, X. Hong, Y. Yang, X. Tang, Y. Zhu and T. Li, *ChemistrySelect*, 2020, **5**, 3201–3207.
36 P. Deepa and P. Philominathan, *Pramana*, 2016, **87**, 100.
37 T. Kato, G. Okada and T. Yanagida, *Radiat. Meas.*, 2016, **92**, 93–98.
38 M. Sterrer, O. Diwald and E. Knözinger, *J. Phys. Chem. B*, 2000, **104**, 3601–3607.
39 A. Palmqvist, M. Wirde, U. Gelius and M. Muhammed, *Nanostruct. Mater.*, 1999, **11**, 995–1007.
40 L. Liu, B. McAllister, H. Ye and P. Hu, *J. Am. Chem. Soc.*, 2006, **128**, 4017–4022.
41 S. Giannakis, M. I. P. López, D. Spuhler, J. A. S. Pérez, P. F. Ibáñez and C. Pulgarin, *Appl. Catal., B*, 2016, **198**, 431–446.
42 D. Zhang, Y. Lin, S. Song, P. Zhang and H. Mi, *J. Theor. Comput. Chem.*, 2018, **17**, 1850018.
43 S. Makhluf, R. Dror, Y. Nitzan, Y. Abramovich, R. Jelinek and A. Gedanken, *Adv. Funct. Mater.*, 2005, **15**, 1708–1715.

© 2021 The Author(s). Published by the Royal Society of Chemistry